Quantum-mechanical calculations of zircon to scheelite transition pathways in $ZrSiO_4$

M. Flórez, J. Contreras-García, and J. M. Recio*
Departamento de Química Física y Analítica and MALTA-Consolider Team, Universidad de Oviedo, E-33006 Oviedo, Spain

M. Marqués
SUPA, School of Physics and Centre for Science at Extreme Conditions, The University of Edinburgh, Edinburgh EH9 3JZ, United Kingdom

(Received 23 December 2008; revised manuscript received 26 January 2009; published 3 March 2009)

Based on accurate quantum-mechanical calculations, a microscopic analysis of mechanistic aspects in the pressure-induced zircon⇌scheelite phase transition of $ZrSiO_4$ is performed under a martensitic scheme at the thermodynamic boundary. Gibbs energy profiles, atomic displacements, bonding reconstruction, and lattice strains are computed across two different transition pathways. After application of a minimum displacement criterion to the atomic positions of consecutive steps in the proposed paths, the trajectories of the 24 atoms involved in each of the unit cells are disclosed. Using the common $I4_1/a$ symmetry, we show that the group-subgroup relationship between two phases displaying the same metal coordinations is not a sufficient condition to characterize a phase transformation as displacive. A very high activation barrier (236 kJ/mol) accompanies the breaking and formation of four primary Zr-O bonds with oxygen displacements as large as 1.29 Å from the zircon to the scheelite structure for this tetragonal path. A lower activation energy (80 kJ/mol) is required to nucleate the scheelite phase from zircon according to our fully optimized monoclinic $C2/c$ transition path. Only two oxygen atoms surrounding Zr have similar displacements in this mechanism, yielding the breaking and formation of two primary Zr-O bonds and revealing the reconstructive character of the transformation. Interestingly enough, SiO_4 tetrahedra are preserved with similar bond lengths and angles when rotating from the zircon to the scheelite phase across the more favorable monoclinic transition pathway.

DOI: 10.1103/PhysRevB.79.104101 PACS number(s): 61.50.Ks, 61.50.Ah, 64.60.A−, 81.30.Hd

I. INTRODUCTION

Attention toward thermodynamic and kinetic aspects of the pressure-induced zircon⇌scheelite phase transition has been recently renewed due to the intrinsic interest in the zircon prototype $ZrSiO_4$ material, which is the most uncompressible material with the ubiquitous SiO_4 tetrahedra, and to the wide range of applications displayed by many isostructural ABO_4 compounds, including their use as host matrices for the immobilization of radioactive wastes.[1–6] Among these works, a previous phase-transition mechanism proposed by Kusaba *et al.*[7] in $ZrSiO_4$ was specifically invoked to interpret a variety of experiments: magnetic changes in $YCrO_4$,[3] alteration by radiation damage of $ZrSiO_4$ phase stability ranges,[2,8] and the enhanced symmetry induced by reduction in particle sizes in $CaWO_4$ nanocrystallites.[9,10] The limited information derived from Kusaba's shock loading experiments makes pertinent a global first-principles simulation to address the proposed mechanism in a more general context, thus providing detailed information of energetic barriers and of the local atomic reorganization taking place across the zircon⇌scheelite transition path.

From a fundamental perspective, the zircon⇌scheelite pressure-induced phase transition in $ZrSiO_4$ exhibits a paradigmatic case to study the nature of the transformation mechanism since the space group of the scheelite-type lattice (reidite from now on, $I4_1/a$) is a subgroup of that of zircon ($I4_1/amd$); and the fourfold and eightfold oxygen coordinations of, respectively, Si and Zr, are present in both structures. These two distinctive features characterizing displacive phase transitions may introduce some confusion when interpreting Kusaba's mechanism.[3,8] A number of experimental results points, however, toward a reconstructive conversion that displays a volume collapse around 10% and pressure-dependent thermal activation barriers for the direct transition around 1000 K at 10 GPa (Refs. 11–13) and 300 K at 20–23 GPa (Refs. 14 and 15), and 1273 K at 0 GPa for the reverse reidite→zircon transformation.[16]

In a recent combined experimental-theoretical work, we have reported on the pressure behavior of zircon, reidite, and postscheelite phases of $ZrSiO_4$ with special emphasis on the equations of state and the relative thermodynamic stability of these structures.[17] In addition, we have very recently presented preliminary results on the characterization of the zircon⇌reidite phase-transition mechanism.[18] In particular, in this last reference, we used a semiempirical approach to evaluate the thermal barrier at the equilibrium zircon-reidite boundary from the observed temperatures at which the zircon⇌reidite transformation occurs when zircon is overpressurized or the zircon structure is recovered from reidite at zero pressure after pressure is released.

In the present paper, we focus on a detailed microscopic description of the energetic, bonding, and structural progressive changes that take place across the transition pathway connecting both structures. The microscopic mechanism of the transition is described considering that the atoms throughout the crystal are displaced simultaneously and coherently from the zircon to the reidite structure (or vice versa) following a transition pathway characterized by a specific space group. One transformation coordinate can be chosen to connect both structures in the same sense that a reaction coordinate monitors the mechanism of a chemical reaction. In spite of the obvious limitations, this martensitic modelization has shown to provide a valuable microscopic

interpretation for many of the physical and chemical processes across phase transformations whether they display a displacive or reconstructive nature.[19–22]

Under both the static approximation and the local-density approximation (LDA) of the density-functional formalism, we have performed accurate quantum-mechanical calculations, with full geometrical optimizations, to investigate two different zircon⇌reidite phase-transition mechanisms: a direct tetragonal ($I4_1/a$) pathway originated by the group-subgroup relationship between zircon and reidite structures, and the highest-symmetry common monoclinic unit cell suggested by Kusaba *et al.*[7] Energetic, bonding, and structural proofs are examined to discriminate among different transition pathways at the thermodynamic transition pressure. The comparison of the semiempirical barrier calculated in Ref. 18 with those values computed in the present microscopic approach allows us to disclose the role of nonmartensitic factors on the transition mechanisms. Whether the cation polyhedra (SiO_4 and ZrO_8) involve or not the same cation-oxygen bonds in zircon and reidite, i.e., if there is or no breaking and formation of bonds across the phase transition, and how bond reconstruction correlates with the energetic barriers are fundamental questions addressed in this paper.

Having a number of atoms as great as 24 in each of the unit cells involved in the two mechanisms, the identification and labeling of the atoms across the phase-transition pathways may become a difficult task, and a possible source of errors if visual procedures are used or the structural data coming out from standard solid-state computational packages are not carefully handled. This is especially relevant if the atomic positions exhibit noticeable changes in passing from one value of the transformation coordinate to the next one, as sometimes happens in the case of the mechanisms studied in this work. For these reasons, we have followed a minimum displacements criterion, equivalent to that used in crystallographic programs, to establish the correspondence between atoms in the initial and final structures of a phase transition,[23–25] to help us to identify, and to label the atoms at each value of the transformation coordinate. This information constitutes an essential ingredient to know how interatomic distances evolve during the phase transition and, consequently, how the bond reorganization takes place. At the very last stage of our work, we have been aware of a very recent theoretical publication dealing with the mechanism of the zircon⇌reidite transition.[5] From a complementary perspective, this reference contains a rigorous symmetry analysis of possible transition pathways that is in general qualitative agreement with our investigation. Nevertheless, two main differences should be remarked concerning the calculations from Smirnov *et al.*:[5] (i) transition paths are evaluated at pressures different from their computed thermodynamic boundary, mainly, at zero pressure, and (ii) the energetics of the transition mechanisms are calculated using an empirical shell model.[26]

The present paper is organized in three more sections and an Appendix collecting the algebra of transformation and strain matrices of the different symmetries involved in the mechanisms. Section II contains crystal data, computational details, a brief summary of our previous results on zircon, reidite, and the zircon⇌reidite transformation, and the definition of the mechanisms studied in this work. Section III presents detailed results and the discussion on the calculated energetic profiles, bonding reorganization and structural changes across the transition pathways. The paper ends with the main conclusions of our work.

II. COMPUTATIONAL DETAILS AND MODELS FOR ZIRCON⇌REIDITE PHASE-TRANSITION MECHANISMS

A. Computational details and previous results on $ZrSiO_4$ polymorphs

Zircon and reidite structures have been described in detail previously (see for example Refs. 27 and 28, and references therein). They belong, respectively, to the $I4_1/amd$ and $I4_1/a$ space groups. Their conventional unit cells are tetragonal and contain four Zr and Si atoms at special positions (Zr at $4a(0,\frac{3}{4},\frac{1}{8})$ and $4b(0,\frac{1}{4},\frac{5}{8})$, and Si at $4b(0,\frac{3}{4},\frac{5}{8})$ and $4a(0,\frac{1}{4},\frac{1}{8})$, respectively) and 16 O atoms at $16h(0,y^z,z^z)$ and $16f(x^r,y^r,z^r)$, respectively. Distorted SiO_4 tetrahedra and distorted ZrO_8 triangular dodecahedra are present in both polymorphs. For the SiO_4 tetrahedra the four Si-O distances are equal, whereas for the ZrO_8 dodecahedra two sets of Zr-O distances, each of them with a multiplicity of 4 are found. In the zircon structure, ZrO_8 and SiO_4 polyhedra alternate to form chains through edge sharing, whereas in reidite ZrO_8 and SiO_4 are linked by corners (see Fig. 1).

In Ref. 17, we presented the results of a combined experimental and theoretical investigation aimed to determine structural and equation of state (EOS) parameters and phase stability thermodynamic boundaries of $ZrSiO_4$ polymorphs. Most of the calculations were performed under the static approximation (zero-temperature and zero-point vibrational contributions neglected). Total-energy calculations at selected unit-cell volumes of a given structure were performed under the framework of the density-functional theory using the Vienna *ab initio* Simulation Package (VASP) code[29] in connection with the projector-augmented wave (PAW) method.[30] The exchange and correlation energies were treated via the LDA and the generalized gradient approximation (GGA) using the Perdew-Wang and the Ceperley-Alder parametrizations,[31,32] respectively. In both cases, high-precision calculations with a cut-off energy of 500 eV for the plane-wave basis and converged with respect to the k-point integration were performed. In particular, the Brillouin-zone integrations were carried out using the special k-point sampling of the Monkhorst-Pack type[33] with $4\times4\times4$ grids. The optimization of the geometry at each volume was performed via a conjugate-gradient minimization of the total energy using the Hellmann-Feynman forces on the atoms and stresses on the unit cell. For the energy calculation of the optimized crystal structures, the tetrahedron method with Blöchl correction was applied. In special, the total energies were converged to less than 0.1 meV/atom and the geometry relaxation was considered to be completed when the total force on the atoms was less than 1 meV/Å. The calculated energy-volume (per formula unit) points (E,V) were converted into static (p,V) isotherms using numerical and analytical EOS fitting procedures coded in the GIBBS program.[34] We compared the pressures so obtained with the values provided by

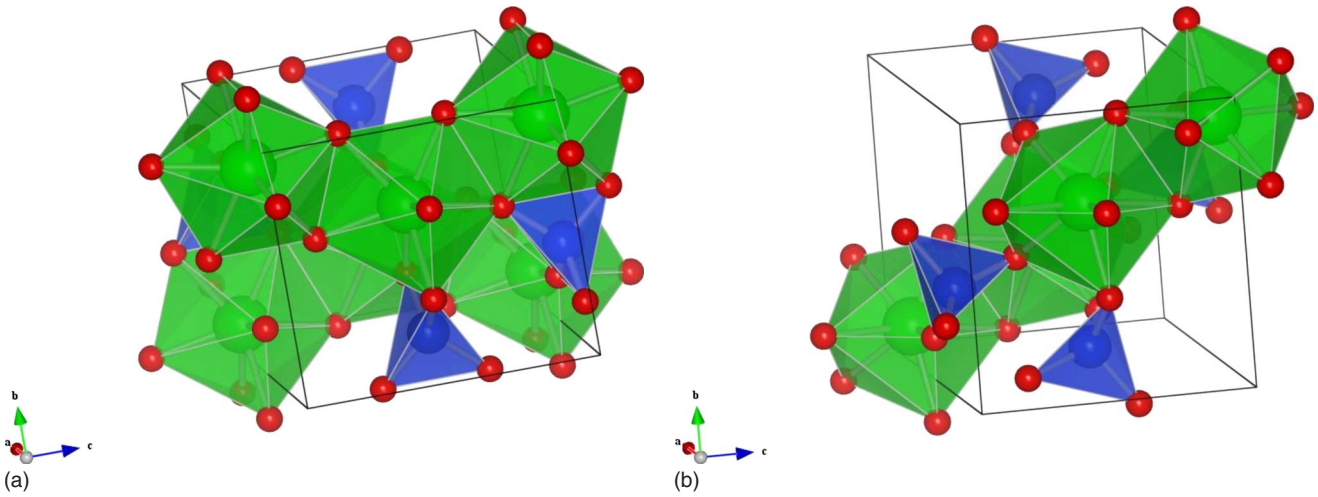

FIG. 1. (Color online) In the zircon structure (left), ZrO_8 and SiO_4 polyhedra (in green and blue, respectively) alternate to form chains through edge sharing, whereas in reidite ZrO_8 and SiO_4 are linked by corners. Balls (in red) stand for oxygen atoms.

the VASP code, where pressures are calculated by averaging the total stress tensor (and adding the Pulay stress) at the optimized geometry. For all the computed volumes, differences were always less than 1 GPa. Furthermore, root-mean-square values of Vinet EOS fittings to our computed p-V data were always greater than 0.999 in both phases.

Our calculated lattice parameters, oxygen coordinates, and EOS parameters at zero pressure for zircon and reidite structures are collected in Table I of Ref. 17 along with representative experimental data (including our own experimental results on zircon). At the LDA level, the expected underestimation of the structural parameters is only within 1%, whereas GGA overestimates up to 4% the observed volume of $ZrSiO_4$ polymorphs. Smirnov *et al.*[5] calculated lattice parameters show a slighter greater deviation (up to 3%) than our LDA values when compared to the experimental data. Concerning B_0, two different sets of experimental values are found in the literature, near to 230 GPa and to 200 GPa, respectively. Our calculated p-V and p-V/V_0 curves are shown in Fig. 2 of Ref. 17 along with relevant experimental data, the second diagram classifying more clearly the curves according to their B_0 values. The p-V diagram [Fig. 2(a) of Ref. 17] shows an overall good agreement between our LDA p-V data and the experiments (in particular, those by van Westrenen *et al.*[15] up to around 15 GPa), the GGA calculations providing volumes about 5% higher.

Besides, we found very good agreement between our diamond-anvil cell and calculated LDA $(p, V/V_0)$ values, both yielding B_0 around 230 GPa. Similarly, B_0 value from the LDA calculations of Farnan *et al.*[35] is 228 GPa. It is also to be said that our GGA p-V/V_0 results are in fair agreement with the measured points of van Westrenen *et al.* [Fig. 2(b) of Ref. 17] from which a B_0 value of 201 GPa is obtained. For reidite, the difference between the two experimental values of B_0 [392 ± 9 (Ref. 13) and 301.4 ± 12.5 (Ref. 36)] is as large as around 100 GPa. These two values are much higher than our computed ones [258 GPa (LDA) and 221 GPa (GGA)], and then, LDA and specially GGA results produce a too compressible scheelite-type polymorph. To end up the summary of our previous thermodynamic study, the LDA static value for the zircon⇌reidite equilibrium transition pressure p_{tr} was computed around 5.3 GPa, a value in good agreement with the extrapolated athermic value from Ono *et al.*[37] high-temperature experiments (6.5 GPa). Our GGA transition pressure of 11.2 GPa is far from these values. To show consistency in our calculations, very similar p_{tr} values (6.2 and 11.4 GPa) were also reported by Farnan *et al.*[35] at LDA and GGA levels of calculation, respectively. In the study of Smirnov *et al.*,[5] their interatomic shell-model simulations yield $p_{tr}=10$ GPa, whereas their GGA value is 15 GPa.

We have also evaluated the thermal barrier at the calculated p_{tr} (see Fig. 1 in Ref. 18) by taking the activation energy associated with this barrier ($\Delta G^{\ddagger}$) as the available vibrational energy of the solid at the temperature needed to observe the direct or reverse transformation in pressure load or unload processes and using a linear hypothesis for $\Delta G^{\ddagger}(p)$.[18] A good estimation of such barrier heights was obtained by coupling a Debye-type model developed in our laboratory[34] to our static total-energy LDA calculations. The value estimated for $\Delta G^{\ddagger}(p_{tr})$ using this strategy, 133 kJ/mol, compares well with a thermal barrier of around 1200 K observed in the experiments Ono *et al.*[13] This value of $\Delta G^{\ddagger}(p_{tr})$ will be compared in Sec. III with those obtained from the Gibbs energy profiles computed in this work. The latter are obtained at zero temperature and neglecting zero-point vibrational contributions using the same computational strategy discussed above (LDA calculations, plane-wave–pseudopotential scheme, and VASP code). Only LDA calculations are considered as they were shown to provide a reasonable overall description of the structure, the compressibility, and the phase transition properties of $ZrSiO_4$.[17,18] Results at LDA level of computation have been also reported in our previous work on group IV nitrides[38] using the same VASP methodology.

B. Models for zircon⇌reidite phase-transition mechanisms

In the present microscopic study of the zircon⇌reidite transformation at the thermodynamic transition pressure, we

TABLE I. Transformation matrices of the lattice vectors (3×3 matrix **P**, first row) and origin shifts (column matrix **p**, second row) associated with the tetragonal and monoclinic (both $P\bar{1}$ and $C2/c$ reference frames) pathways studied in this work (see text). Changes in row are denoted by slashes. I and II stand for zircon and reidite conventional unit cells. Atomic positions for these pathways are also given.

$I4_1/amd(\mathrm{I})\rightarrow I4_1/a$	$I4_1/amd(\mathrm{I})\rightarrow P\bar{1}$	$I4_1/amd(\mathrm{I})\rightarrow C2/c$
(100/010/001)	(001/100/010)	$(-11\frac{1}{2}/-1-1\frac{1}{2}/00\frac{1}{2})$
$(0/\frac{1}{2}/0)$	(0/0/0)	$(\frac{1}{4}/\frac{3}{4}/\frac{1}{4})$
$I4_1/a(\mathrm{II})\rightarrow I4_1/a$	$I4_1/a(\mathrm{II})\rightarrow P\bar{1}$	$I4_1/a(\mathrm{II})\rightarrow C2/c$
(100/010/001)	$(\frac{1}{2}1\frac{1}{2}/-\frac{1}{2}1-\frac{1}{2}/-\frac{1}{2}0\frac{1}{2})$	(−100/−101/010)
$(0/0/\frac{1}{2})$	$(0/0/\frac{1}{2})$	$(-\frac{1}{2}/-\frac{1}{2}/0)$
Zr $4a(0,\frac{1}{4},\frac{1}{8})$	$2\times2i(x_{\mathrm{Zr}},y_{\mathrm{Zr}},z_{\mathrm{Zr}})$	$4e(0,y_{\mathrm{Zr}},\frac{1}{4})$
Si $4b(0,\frac{1}{4},\frac{5}{8})$	$2\times2i(x_{\mathrm{Si}},y_{\mathrm{Si}},z_{\mathrm{Si}})$	$4e(0,y_{\mathrm{Si}},\frac{1}{4})$
O $16f(x_{\mathrm{O}},y_{\mathrm{O}},z_{\mathrm{O}})$	$8\times2i(x_{\mathrm{O}},y_{\mathrm{O}},z_{\mathrm{O}})$	$2\times8f(x_{\mathrm{O}},y_{\mathrm{O}},z_{\mathrm{O}})$

have first chosen a $I4_1/a$ common unit cell with four formula units to describe the mechanism since the space group of reidite ($I4_1/a$) is a subgroup of that of zircon ($I4_1/amd$). Second, we use $P\bar{1}$ and $C2/c$ unit cells with four formula units to study the two-step mechanism proposed by Kusaba *et al.*[7] According to these authors, the volume is reduced to the value of the reidite phase in the first step, whereas in the second step slight atomic displacements provide the final high-pressure structure; and both steps may be carried out simultaneously. In this model, the [110] direction of the zircon structure is converted by simple shearing to the [001] direction of the scheelite structure.[7,39] Here, we use the $P\bar{1}$ reference frame to simulate the distortion of the unit cell of the zircon structure proposed by Kusaba *et al.*:[7] a change in the intersecting angle between [100] and [010] from 90° to 115°.

In Table I, we show the transformation matrices of the lattice vectors (3×3 matrix **P**) and origin shifts (column matrix **p**) associated with the two pathways studied in this work, as well as the atomic coordinates in these paths. The tetragonal common cell (tet) is characterized by specifying five parameters: the two-unit cell lengths ($a_{\mathrm{tet}}, c_{\mathrm{tet}}$) and the three coordinates of its only one nonequivalent oxygen atom. The monoclinic cell (m) is characterized by specifying 12 parameters: the four-unit cell lattice parameters (a_m, b_m, c_m, and β_m), the y coordinate of its only one nonequivalent Zr and Si, and the three coordinates of its two nonequivalent O atoms (O_1 and O_2). The triclinic cell (t) is characterized by specifying the six unit-cell lattice parameters (a_t, b_t, c_t, α_t, β_t, and γ_t) and the three coordinates of its 12 nonequivalent atoms (two Zr, two Si, and eight O).

According to the transformation matrices appearing in Table I, lattice parameters, cell angles and Zr, Si, and O atomic coordinates of zircon and reidite in the common unit cells are easily derived from their corresponding values in the conventional cells. In Table II, we collect the values of the cell parameters of zircon and reidite in these common cells at the zircon⇌reidite transition pressure, according to our static LDA calculations. In Table II we also show the corresponding values of the atomic coordinates in the $I4_1/a$ and $C2/c$ common cells. Details of matrix transformations are given in the Appendix. For each pathway, the correspondence between atoms in zircon and reidite is that providing the minimum distances $\delta_0(i-j)$ between the atoms in both structures (atom i in one structure and atom j in the other one), calculated using the cell parameters of zircon (subscript 0).[23,24] These minimum displacements are shown in Table III for both the tetragonal and monoclinic pathways.

The (symmetrical) Lagrangian finite strain tensor[40] η associated with the zircon→reidite transformation at p_{tr} is

TABLE II. Transition pressure structural properties (cell parameters and atomic positions) of zircon and reidite for the tetragonal and monoclinic (both $P\bar{1}$ and $C2/c$ reference frames) mechanisms. For all of them, $\alpha=\gamma=90°$. See Table I for the values of x_{Zr}, z_{Zr}, x_{Si}, and z_{Si}. See text for the discussion on the correspondence between atoms in zircon and reidite structures. Properties of the monoclinic transition state (TS) are also included. a, b, and c in Å. β in degree.

	$I4_1/a$		$P\bar{1}$			$C2/c$		
	Zircon	Reidite	Zircon	TS	Reidite	Zircon	TS	Reidite
a	6.545	4.696	6.545	5.993	6.139	9.256	7.379	6.641
b	6.545	4.696	5.930	6.590	6.641	9.256	9.445	10.327
c	5.930	10.327	6.545	5.993	6.139	5.496	4.947	4.696
β	90	90	90	104	114.51	147.35	138.24	135.00
y_{Zr}	$\frac{1}{4}$	$\frac{1}{4}$				0.125	0.1205	0.125
y_{Si}	$\frac{1}{4}$	$\frac{1}{4}$				0.625	0.6348	0.625
x_{O_1}	0	0.8424				0.4120	0.6449	0.6576
y_{O_1}	0.5653	0.4916				0.2174	0.2076	0.2044
z_{O_1}	0.1946	0.2956				0.8892	0.1427	0.1492
x_{O_2}						0.7273	0.7428	0.7416
y_{O_2}						0.5327	0.5408	0.5456
z_{O_2}						0.8892	0.8481	0.8340

TABLE III. Transition pressure linear strain finite tensor (η), strain (S) and minimal displacements of the atoms [$\delta_0(i-j)$] in reidite for the tetragonal and monoclinic (both $P\bar{1}$ and $C2/c$ reference frames) mechanisms. Properties of some monoclinic intermediate states are also included. Zircon is taking as the reference structure. See text for definitions of η, S, and $\delta_0(i-j)$. $\delta_0(i-j)$ in Å.

	$I4_1/a$		$P\bar{1}$			$C2/c$	
	Reidite	$\beta_t=102°$	TS	Reidite	$\beta_t=102°$	TS	Reidite
η_{11}	−0.2426	0.0012	−0.0804	−0.0601	−0.1030	−0.1819	−0.2426
η_{22}	−0.2426	0.0038	0.1177	0.1271	0.1053	0.0211	0.1223
η_{33}	1.0162	0.0012	−0.0804	−0.0601	0.0038	0.1177	0.1271
η_{13}	0	−0.1042	−0.1015	−0.1825	0	0	0
S	0.3575	0.0491	0.0726	0.1000	0.0491	0.0726	0.1000
δ_0(Zr-Zr)	0	0.0001	0.0419	0	0.0001	0.0419	0
δ_0(Si-Si)	0	0.0008	0.0906	0	0.0008	0.0906	0
$\delta_0(O_1\text{-}O_1)$	1.2866	0.0309	1.2370	1.3246	0.0309	1.2370	1.3246
$\delta_0(O_2\text{-}O_2)$		0.0307	0.3654	0.4381	0.0307	0.3654	0.4381

also collected in Table III. The orthonormal reference frame [$(\vec{e}_1, \vec{e}_2, \vec{e}_3)$, where $\vec{e}_1$ stands for the unitary vector along the x axis and so on] chosen for the evaluation of η has the following orientation with respect to the conventional cell zircon frame (I): $\vec{e}_1$, $\vec{e}_2$, and $\vec{e}_3$ are parallel to $\vec{a}_I$, $\vec{b}_I$, and $\vec{c}_I$, respectively, for the $I4_1/a$ cell; to $\vec{b}_I$, $\vec{c}_I$, and $\vec{a}_I$, respectively, for the $P\bar{1}$ cell; and to $\vec{a}_I+\vec{b}_I$, $\vec{a}_I-\vec{b}_I$, and $\vec{c}_I$, respectively, for the $C2/c$ cell.

Note in Table III that $\eta_{13}(C2/c)$ is zero, the diagonal elements of $\eta(C2/c)$ being the eigenvalues of $\eta(P\bar{1})$ (its principal strains) and $\vec{e}_1$, $\vec{e}_2$, and $\vec{e}_3$ for $C2/c$ being the corresponding principal directions. One of them ($\vec{e}_2$) is parallel to the unique monoclinic axis. More details on the chosen orthonormal reference frame and the structure of the η matrices are also given in the Appendix. The parameter S included in Table III is a measure of the lattice distortion defined as the square root of the sum of squared eigenvalues of strain tensor η divided by 3.[23,24]

The purpose of analyzing the atomic displacements and the strain tensor involved in the mechanisms is obvious: small values of $\delta_0(i-j)$ and S suggest an *a priori* competitive mechanism. Thus, based on this argument, the monoclinic mechanism is expected to be preferred to the tetragonal one because it implies: (i) a rather smaller lattice strain and (ii) very similar atomic displacements for one half of the oxygen atoms, and values of about one third for the other half. The bigger value of S in the tetragonal pathway comes mainly from the large elongation along the c axis of zircon needed to achieve the scheelite structure in this mechanism as the [001] direction of the zircon structure is changed into the [001] direction in the scheelite structure[7] (note the high value of η_{33} in the $I4_1a$ cell). Of course, we must stress that a rigorous conclusion on the more favorable mechanism at a given pressure and temperature requires the comparison of the corresponding calculated Gibbs energy profiles, one of the tasks performed in Sec. III.

The $I4_1/a$ tetragonal transition path may be walked using either the O position or the c/a ratio as the transformation coordinate. For computational reasons, we have chosen c/a, which evolves from 0.9059 (zircon) to 2.1990 (reidite) at p_{tr}, and at each value of this coordinate we optimized the unit cell lattice parameter a_{tet} and O coordinates. Our second approach to the zircon⇌reidite mechanism was the evaluation of the $C2/c$ transition pathway. At the transition pressure, the calculation of the Gibbs energy profile is performed in the triclinic $P\bar{1}$ reference frame using the angle β_t as the transformation coordinate. The unit-cell parameters a_t and b_t and atomic positions are optimized at several values of this coordinate, which evolves from 90° (zircon) to 114.51° (reidite) at p_{tr}, while maintaining α_t and γ_t fixed to 90° and a_t equal to c_t. The results obtained correspond to a full optimization of the $C2/c$ monoclinic common cell introduced in Table I. The conversion is easily carried out by using the following $P\bar{1}\rightarrow C2/c$ transformation matrices of the lattice vectors (first matrix, 3×3 matrix **P**) and origin shifts (second matrix, column matrix **p**): $(-1\ -1\ \frac{1}{2}/0\ 0\ \frac{1}{2}/-1\ 1\ \frac{1}{2})$ and $(\frac{3}{4}/\frac{1}{4}/\frac{1}{4})$.

III. RESULTS AND DISCUSSION: TETRAGONAL AND MONOCLINIC PATHWAYS

A. Gibbs energy profiles

Let us discuss and compare now the tetragonal and monoclinic pathways connecting zircon and reidite at the LDA static value of the thermodynamic transition pressure (5.3 GPa). The Gibbs energy profiles of both mechanisms are shown in Fig. 2, where G (relative to its value in zircon and reidite) is represented versus a normalized transformation coordinate ξ evolving from 0 (zircon) to 1 (reidite) and defined as follows: $\xi_{tet}=[(c/a)-(c/a)_{zircon}]/[(c/a)_{reidite}-(c/a)_{zircon}]$, for the tetragonal pathway, and $\xi_t=(\beta_t-\beta_{t,zircon})/(\beta_{t,reidite}-\beta_{t,zircon})$ for the monoclinic one.

Three conclusive remarks can be drawn from Fig. 2: (i) the $\Delta G(\xi)$ profile for the tetragonal pathway is more symmetric and soft than that for the monoclinic one, (ii) the transition states appear at around $\xi_{tet}=0.4$ (tetragonal path-

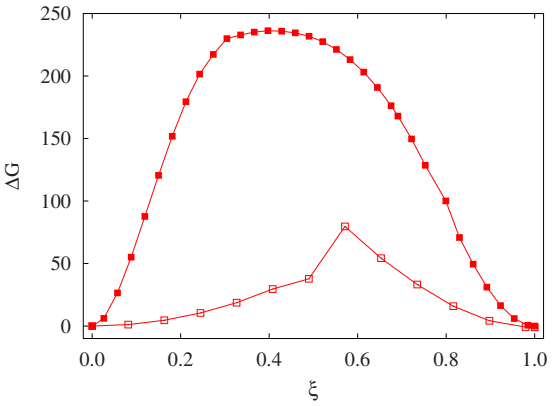

FIG. 2. (Color online) Gibbs energy profiles for the tetragonal $I4_1a$ (solid squares) and monoclinic $C2/c$ (open squares) transition paths of the zircon→reidite transformation at p_{tr}. ξ stands for the reduced transformation coordinates ξ_{tet} and ξ_t, respectively (see text).

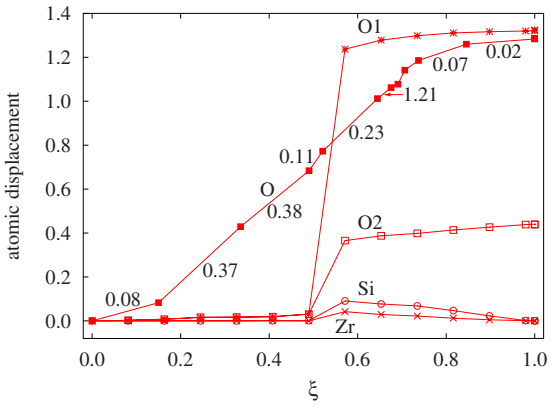

FIG. 3. (Color online) Minimum atomic displacements $\delta_0(i-j)$ in terms of the reduced transformation coordinates for the tetragonal (O, solid curve) and monoclinic (Zr, Si, O_1, and O_2, solid curves) pathways. Some $\delta_{\xi_i}(\xi_{i+1})$ values for the O atom in the tetragonal path are also included in the figure (see text). Displacements in Å.

way) and $\xi_t=0.6$ (monoclinic pathway), and (iii) the activation barrier for the monoclinic pathway is clearly smaller than that for the tetragonal one, thus suggesting that the former is a much more favorable mechanism for the zircon⇌reidite transition at least at the thermodynamic transition pressure. In quantitative terms, the tetragonal pathway shows an activation barrier of 236 kJ/mol, too high compared with our previous estimation (133 KJ/mol) based on the observed temperatures at which the transition is observed at zero and high pressure, whereas the transition state of the monoclinic pathway is only around 80 kJ/mol above zircon and reidite. Given the approximations involved in our martensitic description, this value below the estimation of 133 kJ/mol suggests a contribution to the barrier of about 50 kJ/mol coming from surface and/or diffusion terms associated with a nucleation and growth mechanism and allows us to infer that this transition could have a reconstructive character at least at the thermodynamic transition pressure. This will be confirmed after a more detailed discussion of Fig. 2 in connection with the structural changes across the transition paths given below.

Rigorously speaking, the zircon→reidite transition barriers calculated by Smirnov *et al.*[5] (285 and 144 kJ/mol) cannot be quantitatively compared with our values. Although the two explored paths in their work correspond in essence with our tetragonal and monoclinic mechanisms, respectively, the pressure used in their calculations is 0 GPa, which is neither their nor our calculated transition pressure. Nevertheless, as pressure increases from zero to p_{tr}, a decreasing of the barrier is expected (when $\Delta V^{\ddagger}<0$) yielding values closer to our predictions. In fact, our zero pressure estimation of the activation barrier for the zircon→reidite monoclinic path is 100 and 20 kJ/mol above the corresponding value at p_{tr}.

B. Atomic displacements

It must be noted that due to the high computational cost frequently involved in electronic structure *ab initio* calculations, it is not always possible to dispose of results for an enough dense grid of ξ values. In some systems with complex high dimensional potential-energy surfaces as those studied in this work, this may result in moderate changes in the atomic positions in passing from some values of ξ to the next ones, thus making difficult the task of identification and labeling of the atoms across the phase-transition pathway. The minimum displacements criterion presented above is also used in this context to help us in the identification and labeling of the atoms at each value of the transformation coordinate when some atomic positions change moderately from ξ_i to ξ_{i+1}. In this case, the displacements are calculated using the cell parameters of the structure at ξ_i and are denoted by $\delta_{\xi_i}(\xi_{i+1})$ or simply by $\delta(i-j)$. Note that, as a general rule, a set of small $\delta_{\xi_i}(\xi_{i+1})$ values is an indication of a soft and nearly continuous evolution of all the atomic positions and then of an enough dense grid of ξ values.

In Fig. 3, we show the evolution of the $\delta_0(\xi)$ values (calculated using the cell parameters of zircon) across both transition pathways in terms of the corresponding reduced transformation coordinate (solid curves). Some of these δ_0 values appear in Table III. $\delta_{\xi_i}(\xi_{i+1})$ values for the O atom in the tetragonal path are also indicated in Fig. 3 (those not appearing are less than 0.06 Å). The corresponding values for Zr, Si, O_1, and O_2 in the monoclinic pathway are less than 0.015 Å in the range $90° \le \beta_t \le 102°$ and less than 0.04 Å in the range $104° \le \beta_t \le 114.51°$ due to the nearly constant behavior of the atomic positions in these ranges of β_t. The values of δ(Zr-Zr), δ(Si-Si), δ(O_1-O_1), and δ(O_2-O_2) from $\beta_t=102°$ ($\xi_t=0.49$) to $\beta_t=104°$ ($\xi_t=0.57$), and calculated using the cell parameters of the structure at $\beta_t=102°$, are (in Å): 0.0462, 0.1006, 1.1521, and 0.3362, respectively. Thus, the minimum displacements criterion has been useful to help us to establish the correspondence between O_1 atoms in the $\beta_t=102°$ and 104° structures. The minimum O_1 displacement of 1.1521 Å from $\beta_t=102°$ to $\beta_t=104°$ corresponds to the change in $(x_{O_1}, y_{O_1}, z_{O_1})$ from (0.4124, 0.2147, 0.8866) to (0.6449, 0.2076, 1.1427) [see Fig. 7(d) below]. Furthermore, according to the δ(O-O) values shown in Fig. 3 for the te-

tragonal path, the minimum displacements criterion has been also especially useful to help us to establish the correspondence between O atoms in the $c/a=1.74$ ($\xi_{tet}=0.6446$) and $c/a=1.78$ ($\xi_{tet}=0.6755$) structures of this pathway. The minimum O displacement of 1.2145 Å from $c/a=1.74$ to $c/a=1.78$ (calculated using the cell parameters of the structure at $c/a=1.74$) corresponds to the change in (x_O, y_O, z_O) from (0.1128, 0.4989, 0.2855) to (–0.1201, 0.4963, 0.2881). Of course, the corresponding values of δ(Zr-Zr) and δ(Si-Si), as well as those of δ_0(Zr-Zr) and δ_0(Si-Si), are zero, as the cationic positions are fixed across the tetragonal path.

In both tetragonal and monoclinic analyses, the atomic correspondences obtained from the δ values discussed above are consistent with those obtained in Sec. II from the δ_0 values in passing from zircon to reidite (see Table II). With respect to the evolution of the $\delta_0(\xi)$ values shown in Fig. 3, it is interesting to compare the quite soft increasing obtained for δ_0(O-O) in the tetragonal pathway with the behavior observed for $\delta_0(O_1\text{-}O_1)$ and $\delta_0(O_2\text{-}O_2)$ in the monoclinic one: (i) very small values from zircon to $\beta_t=102°$; (ii) sharp increasing from $\beta_t=102°$ to 104°, especially for $\delta_0(O_1\text{-}O_1)$; and (iii) small increasing from $\beta_t=104°$ to reidite. Note also the small values of δ_0(Zr-Zr) and δ_0(Si-Si) in the whole range of ξ, and particularly for $\beta_t \leq 102°$, in this monoclinic pathway. In this path, the nearly constant behavior of the atomic positions in the range $90° < \beta_t < 102°$, as well as the moderate changes in the lattice parameters in this range of β_t give rise to quite similar values for δ_0 from zircon to $\beta_t=104°$ and for δ from $\beta_t=102°$ to $\beta_t=104°$. Finally, it must be noted that, in spite of the rather large O displacement from $c/a=1.74$ to $c/a=1.78$ in the tetragonal path, due to the important change in x_O in passing from one structure to the another one (see above), the difference between $\delta_0(c/a=1.78)$ and $\delta_0(c/a=1.74)$ is quite small because of the cancellation induced by the x_O change in sign in passing from $c/a=1.74$ to $c/a=1.78$.

C. Bonding reconstruction: Structural and chemical

It is only after the analysis of the atomic displacements when we can determine how primary (valence) bond reorganization takes place across both transition pathways. We have followed the progressive changes in the local geometry and in the electronic structure surrounding Zr and Si atoms. The evolution of relevant Zr-O distances is collected in Figs. 4 and 5. In these figures, curves identify groups of oxygen atoms at the same distance of a given Zr atom across the transition path. We indicate in the figures the number of O atoms associated with each curve in a range of ξ values.

Let us discuss now Figs. 4 and 5 in connection with Fig. 2 introduced above. In spite of the same eightfold coordination of Zr in both zircon and reidite, an analysis of the Zr-O distances across the tetragonal path shows that four Zr-O bonds break and subsequently four new Zr-O bonds emerge (see Fig. 4), the flat activation barrier of this mechanism being related to the fourfold coordination of Zr and to the small values of the nearest Zr-O distances for c/a values around 1.2–1.6 (ξ_{tet} around 0.23–0.54). It must be noted that, in spite of the group-subgroup relation between the symmetries of zircon and reidite, these results on the $I4_1/a$ tetragonal pathway do not correspond to a displacive transformation. Finally, the sharp increase (decrease) in the next-nearest (next-next-nearest) Zr-O distance at $c/a=1.74$ in passing from $c/a=1.74$ ($\xi_{tet}=0.6446$) to $c/a=1.78$ ($\xi_{tet}=0.6755$) is mainly a consequence of the change in x_O discussed above.

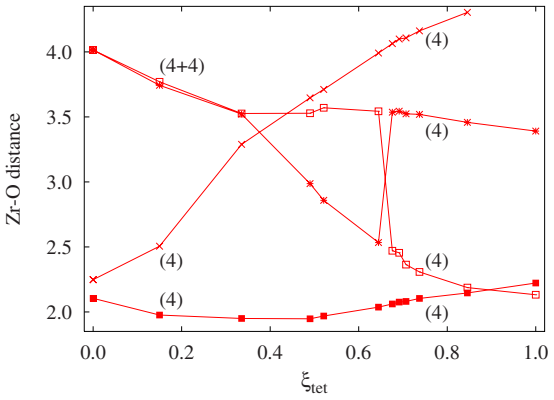

FIG. 4. (Color online) Some Zr-O distances in terms of the reduced transformation parameter for the tetragonal pathway (in Å). In parentheses we show the number of O atoms associated to each curve in a range of ξ values.

The reconstructive character of the transition inferred from energetic considerations in the monoclinic pathway is also provided following the changes in the interatomic distances. According to the evolution of the shortest Zr-O distances depicted in Fig. 5, two Zr-O bonds break and two new Zr-O bonds appear in the mechanism to keep the same cation coordination in both phases. At p_{tr}, this reorganization takes place in the neighborhood of the transition state (from $\beta_t=102°$ to 104°, that is, from $\xi_t=0.49$ to 0.57) and can be associated with the sharp increase in energy in the Gibbs energy profile (see Figs. 2 and 5). In this interval, two Zr-O_1 distances increase from 2.24 to 3.39 Å (two bonds break) and other two decrease from 3.63 to 2.40 Å (two bonds tend to appear), giving rise to a transition state ($\beta_t=104°$) with a 4+2(+2)-coordinated Zr: four O atoms (two O_1 and two O_2) at 2.11 Å, two O_2 atoms at 2.15 Å, and two O_1 atoms at

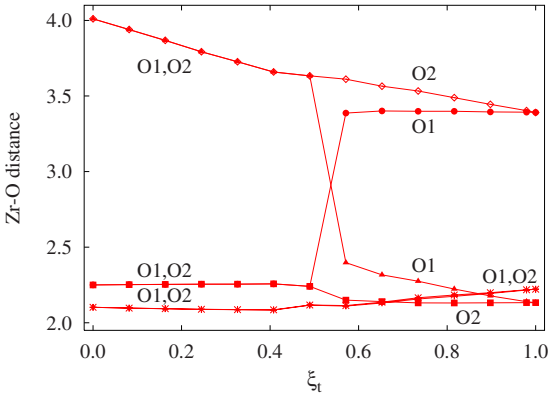

FIG. 5. (Color online) Some Zr-O distances in terms of the reduced transformation parameter for the monoclinic pathway (in Å). The number of O_1 (and O_2) atoms associated to each curve in a range of ξ values is two.

2.40 Å, the latter being not strictly bonded to the Zr atom in this state (see our chemical analysis below). From $\beta_t=104°$ to 114.51°, the structure evolves to achieve the 4+4 coordination in reidite, the two next-next-nearest O_1 neighbors in the transition state becoming closer and closer to the Zr atom to finally appear included between the four nearest O neighbors in reidite (with a Zr-O distance of 2.13 Å). Thus, the 4+4 coordination of Zr in zircon is maintained until it suddenly changes to a 4+2(+2) coordination at the transition state and then gradually evolves to the 4+4 coordination in reidite. We must note that the breaking and formation of Zr-O bonds is related to oxygen of type O_1, that is, those suffering displacements higher than 1 Å in the neighborhood of the transition state.

According to our results, none Si-O bond is broken or formed across the paths studied in this work. The four Si-O distances of the SiO_4 tetrahedra suffer small changes in the monoclinic transition pathway. Their values are about 1.61 Å between $\beta_t=90°$ and 102° and change to 1.657 Å (two Si-O_1 bonds) and 1.648 Å (two Si-O_2 bonds) from $\beta_t=102°$ to 104°. From this transition state, Si-O_2 distances show a decreasing behavior to achieve the value of 1.641 Å in reidite, whereas Si-O_1 distances attain this value by passing through a maximum of 1.660 Å at around $\beta_t=108°$. The increase in 0.035-0.045 Å in the neighborhood of the transition state can be compared with the increase in 0.028 Å in passing from zircon to reidite. On the other hand, if we label the four O atoms surrounding a given Si by O_{1a}, O_{1b}, O_{2a}, and O_{2b}, the values of the O_i-Si-O_j angles (in degree) at, respectively, $\beta_t=90°$, 100°, 104°, and 114.51°, are: 116, 112, 131, and 120 (O_{1a}-Si-O_{1b}); 116, 112, 115, and 120 (O_{2a}-Si-O_{2b}); 116, 122, 100, and 104 (O_{1a}-Si-O_{2a} and O_{1b}-Si-O_{2b}); and 97, 95, 106, and 104 (O_{1b}-Si-O_{2a} and O_{1a}-Si-O_{2b}). Thus, first, we must note that both the O_1-Si-O_1 and O_2-Si-O_2 angles change from 116° in zircon to 120° in reidite but taking different values at the transition state (131° the former and 115° the latter). Second, the changes in the four O_1-Si-O_2 angles from zircon to reidite are dominated by their increase (or decrease) in the neighborhood of the transition state. Nevertheless, Si-O distances and O_i-Si-O_j angles of the SiO_4 units suffer moderate changes across the monoclinic transition pathway, and consequently, it is mainly the breaking and formation of two Zr-O_1 bonds, related to the tilting of the SiO_4 tetrahedra to pass from the sharing with the ZrO_8 bidisphenoid of a O-O edge in zircon to a O corner in reidite, which involves an energy barrier high enough to hinder the phase transformation at ambient temperature.

Further support to the bonding reconstruction process can be gained from the crystalline wave function following the topological analysis of the electron localization function (ELF).[41,42] The ELF is able to identify those regions of the unit cell where electrons are highly localized. Each of these regions is characterized by one maximum or attractor of the ELF. The ELF topological analysis has proven to be a very efficient tool to monitor in an unambiguous manner chemical bonding changes taking place in solid-solid phase transformations. Recent applications for the zinc blende→rock salt and α-cristobalite→stishovite phase transitions in BeO and SiO_2, respectively, have successfully illustrated how the metal coordination increases across the corresponding transition paths.[43,44] In the case of outer core electrons of atoms of the second row and beyond, ELF maxima are disposed in the shell according to a minimization of the repulsion with surrounding valence basins[44] and not merely opposed to ligands as was previously suggested.[45] The representation of ELF maxima in different structures of $ZrSiO_4$ clearly supports this *core shell electron pair repulsion model* (CSEPR), where the outer core electrons of Zr are disposed pointing to the "spare" space in each of the structures (see Fig. 6).

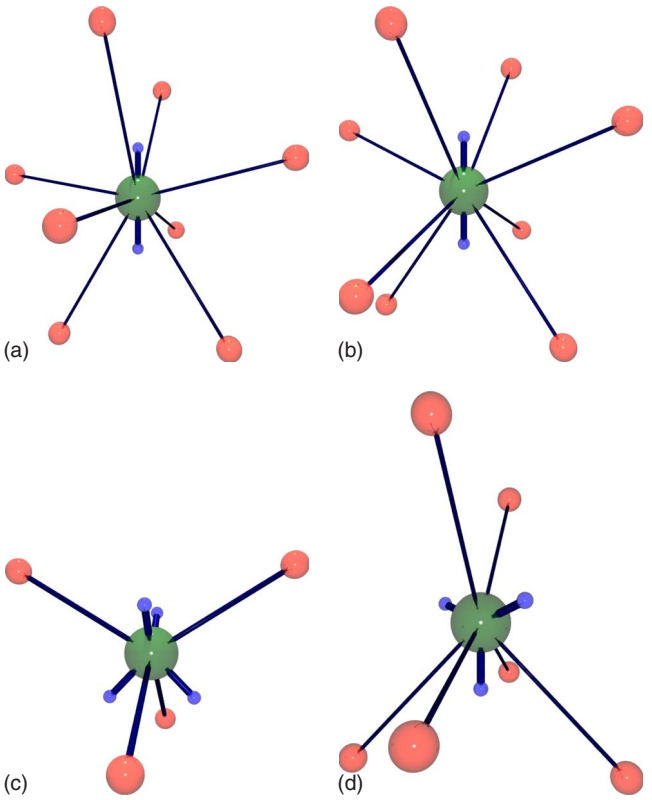

FIG. 6. (Color online) Evolution of ELF maxima of Zr outer core along the tetragonal and monoclinic pathways: zircon (top-left), reidite (top-right), tetragonal intermediate ($\xi_{tet}=0.40$) (bottom-left), and (d) monoclinic intermediate ($\xi_t=0.57$) (bottom-right). Big (green) and medium-size (red) balls stand for Zr and O atoms, respectively, whereas the small balls (blue) emerging from Zr stand for Zr outer core maxima.

Both in zircon and reidite [Fig. 6 (top)], the eightfolded sphere of coordination of Zr is disposed forming two cages of distorted oxygen squared-based pyramids (medium-size balls) being the Zr atom (big balls) the common apex. Hence, the ELF outer core maxima of Zr [*outer core maxima* (OCM)] related to the $3s3p$ electrons occupy the voids in between the cages so that two OCM (two small balls up and down with respect to Zr) are found for both polymorphs. In other words, in both cases the coordination of Zr can be understood as two groups of four oxygen, and each of the OCM pointing at the middle of them so that the main change from one situation to the other is the spatial disposition of oxygen. In the zircon case, oxygen share the same SiO_4 tetrahedron (Fig. 1 left), whereas in the reidite, they belong to different silicon subunits (Fig. 1 right). During the transition, the environment change requires a reconstructive flip of sili-

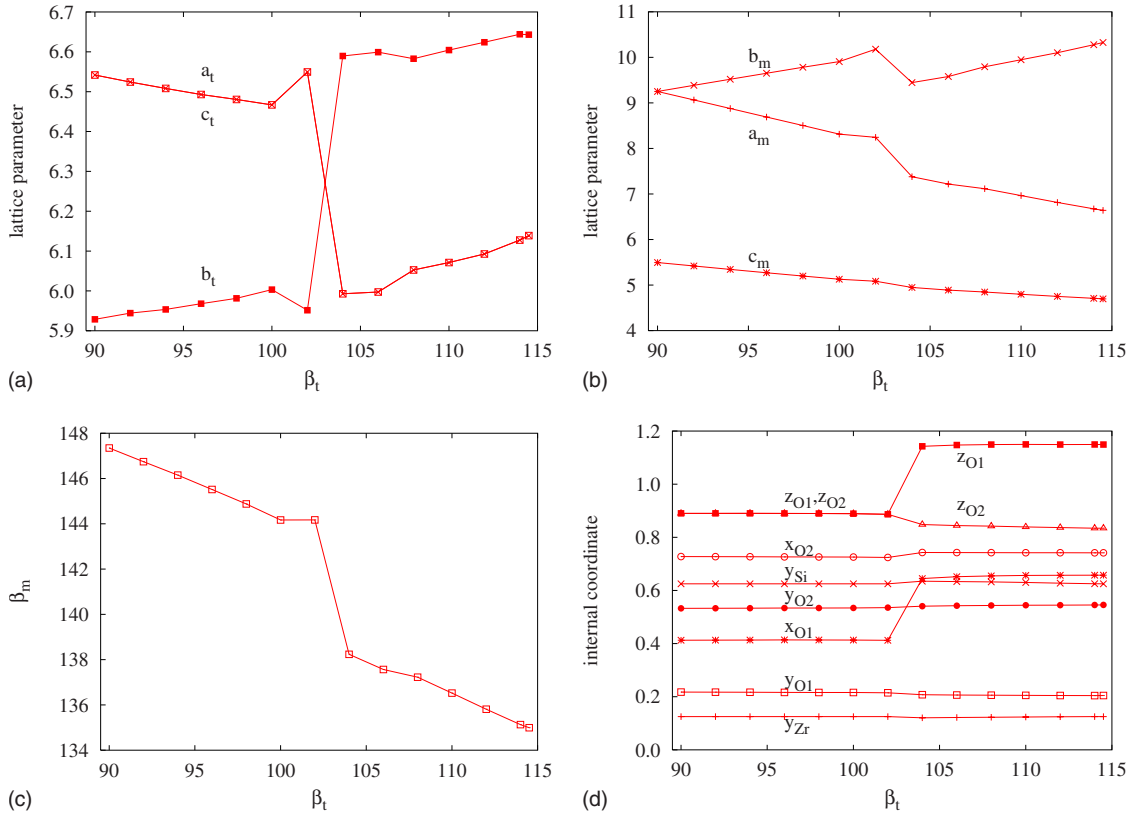

FIG. 7. (Color online) (a) a_t, b_t, and c_t parameters of the triclinic cell (in Å), (b) a_m, b_m, and c_m parameters of the monoclinic cell (in Å), (c) β_m angle of the monoclinic cell (in degree), and (d) positions of the atoms in the monoclinic cell, in terms of the transformation coordinate β_t (in degree) for the monoclinic pathway. x and z for both Zr and Si are fixed ($x=0$ and $z=\frac{1}{4}$ for both atoms).

con tetrahedra. As discussed above, the SiO_4 flip takes place in the neighborhood of the transition state and can be associated with the increase in energy in the Gibbs energy profile.

The disposition of OCM according to the CSEPR reflects in an indirect and subtle way the coordination of elements and, hence, is able to provide insight into ionic interactions, otherwise difficult to handle. Due to the high symmetry of the tetragonal mechanism, the transition state involves the simultaneous rupture of the bonds of the second coordination sphere, as the new O_4 group is approaching. This breaking of bonds can be followed by means of the ELF along the transition pathway. Figure 6 (bottom-left) shows how half of the oxygen have left their original position so that the former two OCMs split in four maxima in a pseudotetrahedral disposition, complementary to that of the remaining oxygen atoms.

The transition along the monoclinic pathway implies the rupture of two bonds, whereas the other six remain in the active coordination of Zr along the transformation. Figure 6 (bottom-right) shows how the transition state associated with the flipping of SiO_4 tetrahedra keeps one of the O_4 cages with its Zr OCM (see the bottom part of the figure). The top part of the coordination maintains two oxygen at their position, whereas two new Zr OCM (small balls) at the top highlight the position of the outgoing ligands and reveal that the two new incoming oxygen are not still bonded with Zr (see discussion above). It can be seen that the monoclinic pathway favors a correct electron localization for the minimal reorganization along the pathway. Moreover, the number of broken bonds along the tetragonal path clearly stands for the suitability of the monoclinic description, where the coordination remains close to that of the stable phases at all points.

D. Cell and inner strains

The changes in distances and angles across the monoclinic pathway discussed above are a consequence of the simultaneous changes in both the lattice parameters and the atomic positions. We detail now the evolution of these properties (see Fig. 7). Changes in the triclinic cell lattice parameters are smooth up to the neighborhood of the transition state where abrupt jumps occur (a_t and b_t values are interchanged when going from $\beta_t=102°$ to $\beta_t=104°$). A change in the trends of the lattice parameters from $\beta_t=100°$ to 102° could reveal some convergency problems in our calculations. The mentioned interchange does not appear in the monoclinic cell reference frame. Here, a_m, b_m, c_m, and β_m show smooth changes (a_m, c_m, and β_m decrease and b_m increases when β_t increases) except for a decreasing jump in a_m, b_m, and β_m when passing from $\beta_t=102°$ to 104°. As a result, volume (not displayed in the figure) follows a continuous and soft decreasing across the transition path from zircon to $\beta_t=100°$, a big decreasing jump from 102° to 104°, and a very soft decreasing from 104° to reidite. Concerning atomic coordinates, and as expected from the discussion above, we find that changes in those for Si and Zr are negligible,

whereas for the oxygen crystallographic coordinates two well-differentiated β_t ranges of a rather constant behavior appear in the transition path enabling the location of the transition state. In the $C2/c$ reference frame, they are x_{O_1} and z_{O_1} which suffer a remarkable jump when passing from $\beta_t = 102°$ to 104°, while y_{O_1} and the O_2 coordinates suffer minor changes. This behavior can be explained as due to the *phase inertia* associated with the high mechanical stability of the two structures, i.e., the lattice parameters and the oxygen coordinates of intermediate monoclinic structures only suffer substantial deviations from the values in the zircon and reidite phases after β_t achieves values in the middle of the transition pathway (that is, for ξ_t values around 0.5).

According to the changes in lattice parameters and atomic coordinates discussed above, the monoclinic mechanism may be seen as a three consecutive "processes" mechanism: (i) zircon lattice deformation (from $\beta_t = 90°$ to 102°); (ii) simultaneous lattice and inner deformations, the latter being related to oxygen displacements from their fractional coordinates in zircon to those in reidite (from $\beta_t = 102°$ to 104°); and (iii) lattice deformation with atoms at new positions to obtain the reidite structure (from $\beta_t = 104°$ to 114.51°). In step (ii), the structure suffers high volume reduction and rather high O_1 displacements. In fact, the main contribution to the zircon $\rightarrow$ reidite volume collapse at p_{tr} (−10.2%) comes from this step (ii), as illustrated by the relative changes of volume from zircon ($\beta_t = 90°$) to: $\beta_t = 100°$ (−2.6%), $\beta_t = 102°$ (−1.6%), and $\beta_t = 104°$ ($\Delta V^{\ddagger} = -9.5\%$). Furthermore, as commented above, the O_1 displacements occurring in step (ii) may be related to the high activation barrier of this mechanism as they are the main responsible of the breaking and formation of the two Zr-O_1 bonds associated with the tilting of SiO_4 tetrahedra. This fact can be illustrated quantitatively here by comparing the actual changes in two Zr-O_1 distances from $\beta_t = 102°$ to 104° with those obtained neglecting the atomic displacements (in parentheses): 2.241 Å changes to 3.387 Å (2.366 Å), and 3.633 Å changes to 2.398 Å (3.335 Å). Overall, it is to be finally noted that, according to our calculations, the role of the oxygen displacements in the monoclinic mechanism seems to be more important than that suggested by Kusaba *et al.*[7]

IV. CONCLUSIONS

We have used a first-principles strategy to calculate two transition pathways connecting zircon and reidite at the zircon-reidite thermodynamic transition pressure. A tetragonal $I4_1/a$ pathway produces an unrealistic description of the transformation mechanism giving rise to a very high activation Gibbs energy and to intermediate structures with tetracoordinated Zr atoms. A previously proposed low-symmetry triclinic unit cell has been shown to correspond to a monoclinic $C2/c$ path that provides a reasonable activation Gibbs energy. The value of the monoclinic barrier (80 kJ/mol) is below our estimation in Ref. 18 using a semiempirical mechanistic model (133 kJ/mol) suggesting the relevance of surface and/or diffusion contributions to the experimental barrier. We have investigated a set of proofs from the bonding point of view that are consistent with discarding the tetragonal mechanism in favor of the monoclinic one, as well as with the reconstructive nature of the transition in $ZrSiO_4$. In the monoclinic mechanism, the analysis of atomic displacements has shown that only two Zr-O bonds are broken previous to the emergence of two new Zr-O bonds. The ELF analysis of the intermediates not only confirms this assumption but it also reveals that the monoclinic intermediate requires a much smaller electronic reorganization than the tetragonal one, where the fourfolded intermediate gives rise to a transition state that is not similar to zircon nor to reidite. Overall, we have shown that energy profiles, atomic displacements, and chemical bonding can all be used and combined in the complex practice of analyzing mechanisms. It is finally to be emphasized that, although the calculations in the present study were only limited to ZrSiO4, these conclusions are of general application to the zircon $\rightleftharpoons$ scheelite phase transition. This transformation is very common in ternary ABO_4 oxides (see for example Ref. 6), and it is of broad interest in geophysics and geochemistry due to the number of minerals adopting the ABO_4 formula and to the applications of zircon in studies on the evolution of Earth's crust and mantle as well as on age dating.[27]

ACKNOWLEDGMENTS

Financial support from the Spanish MICINN and FEDER programs under Project No. MAT2006-13548-C02-02 and the Spanish MALTA-Consolider Ingenio-2010 program under Project No. CSD2007-00045 are gratefully acknowledged. J.C.G. thanks the Spanish MICINN for a FPU postgraduate grant.

APPENDIX

The transformations of the lattice vectors and the coordinates from the conventional to the common cells are as follows:[46] $(\vec{a}_i \vec{b}_i \vec{c}_i) = (\vec{a}_j \vec{b}_j \vec{c}_j)$ **P** and $(x_i/y_i/z_i) = \mathbf{P}^{-1}[(x_j/y_j/z_j) - \mathbf{p}]$, where subscripts i refer to the lattice vectors and coordinates in the common cells and j to these properties in the conventional cells (i=tet, t, and m, where tet, t, and m stand for the tetragonal, triclinic, and monoclinic common cells, respectively, and j=I and II, where I and II stand for zircon and reidite conventional unit cells). The use of the **P** and **p** matrices shown in Table I gives rise to the relationships described in the next paragraph.

At the LDA calculated zircon-reidite transition pressure (p_{tr}=5.3 GPa), the lattice parameters of zircon in the $I4_1/a$ common cell keep the same values as in the $I4_1/amd$ conventional unit cell ($a_{tet} = b_{tet} = a_I = 6.545$ Å and $c_{tet} = c_I = 5.9296$ Å), but Zr, Si, and O display new positions at $(0, \frac{1}{4}, \frac{1}{8})$, $(0, \frac{1}{4}, \frac{5}{8})$, and (0,0.5653, 0.1946), respectively. For the reidite structure in the $I4_1/a$ common cell, $a_{tet} = b_{tet} = a_{II} = 4.696$ Å, $c_{tet} = c_{II} = 10.327$ Å, Zr, and Si are in the same positions as in zircon in this cell but O changes to (0.8424, 0.4916, 0.2956) (see Table II). In the $P\bar{1}$ cell, $a_t = c_t = a_I$, $b_t = c_I$, and $\alpha_t = \beta_t = \gamma_t = 90°$ for zircon, and $a_t = c_t = \sqrt{\frac{1}{2}a_{II}^2 + \frac{1}{4}c_{II}^2}$, $b_t = \sqrt{2}a_{II}$, $\alpha_t = \gamma_t = 90°$, and $\beta_t = \arccos[(\frac{1}{2}a_{II}^2$

$-\frac{1}{4}c_{\mathrm{II}}^2)/(\frac{1}{2}a_{\mathrm{II}}^2+\frac{1}{4}c_{\mathrm{II}}^2)]$, and equal to 114.51° according to our LDA results at p_{tr} for reidite. Finally, in the $C2/c$ unit cell, $\alpha_m=\gamma_m=90°$ in zircon and reidite and β_m changes from 147.35 to 135.00° when passing from the former to the latter. In the $C2/c$ and $P\bar{1}$ unit cells, the atomic coordinates of Zr and Si, respectively, are also the same in zircon and reidite whereas the oxygen have different coordinates in the two structures (see Tables I and II).

The orthonormal reference frame chosen for the evaluation of the Lagrangian finite strain tensor[40] η associated to the transformation from zircon to reidite (and to some intermediate structures) at p_{tr} has the following orientation with respect to the common cell zircon frame: $\vec{e}_1$ parallel to a $\vec{a}$, $\vec{e}_2$ perpendicular to $\vec{a}$ in the plane $(\vec{a},\vec{b})$, and $\vec{e}_3$ perpendicular to $\vec{e}_1$ and $\vec{e}_2$. This implies that, for $\gamma=90°$, $\vec{e}_2$ is parallel to $\vec{b}$. If, besides, $\beta=90°$, $\vec{e}_3$ becomes parallel to a $\vec{c}$ ($\vec{e}_1$ stands for the unitary vector along the x axis and so on). Then, $\vec{e}_1=\vec{a}_{\mathrm{tet}}/a_{\mathrm{tet}}=\vec{a}_{\mathrm{I}}/a_{\mathrm{I}}$, $\vec{e}_2=\vec{b}_{\mathrm{tet}}/b_{\mathrm{tet}}=\vec{b}_{\mathrm{I}}/b_{\mathrm{I}}$, and $\vec{e}_3=\vec{c}_{\mathrm{tet}}/c_{\mathrm{tet}}=\vec{c}_{\mathrm{I}}/c_{\mathrm{I}}$ for the $I4_1/a$ cell, $\vec{e}_1=\vec{a}_t/a_t=\vec{b}_{\mathrm{I}}/b_{\mathrm{I}}$, $\vec{e}_2=\vec{b}_t/b_t=\vec{c}_{\mathrm{I}}/c_{\mathrm{I}}$, and $\vec{e}_3=\vec{c}_t/c_t=\vec{a}_{\mathrm{I}}/a_{\mathrm{I}}$ for the $P\bar{1}$ cell, and $\vec{e}_1=\vec{a}_m/a_m$ and parallel to $\vec{a}_{\mathrm{I}}+\vec{b}_{\mathrm{I}}$, $\vec{e}_2=\vec{b}_m/b_m$ and parallel to $\vec{a}_{\mathrm{I}}-\vec{b}_{\mathrm{I}}$, $\vec{e}_3=1.56065\vec{a}_m/a_m+1.85355\vec{c}_m/c_m$ and parallel to $\vec{b}_t$ and to $\vec{c}_{\mathrm{I}}$, for the $C2/c$ cell. The strain tensor has the diagonal form $(\eta_{11}00/0\,\eta_{11}0/00\,\eta_{33})$ for the tetragonal pathway, the principal direction of the tensor corresponding to the unique eigenvalue $(\vec{e}_3)$ being parallel to the symmetry axis 4 and the form $(\eta_{11}0\,\eta_{13}/0\,\eta_{22}0/\eta_{13}0\,\eta_{33})$ for the monoclinic one.

*Corresponding author: mateo@fluor.quimica.uniovi.es

[1] X. Wang, I. Loa, K. Syassen, M. Hanfland, and B. Ferrand, Phys. Rev. B **70**, 064109 (2004).
[2] U. A. Glasmacher, M. Lang, H. Keppler, F. Langenhorst, R. Neumann, D. Schardt, C. Trautmann, and G. A. Wagner, Phys. Rev. Lett. **96**, 195701 (2006).
[3] Y. W. Long, L. X. Yang, Y. Yu, F. Y. Li, R. C. Yu, and C. Q. Jin, Phys. Rev. B **75**, 104402 (2007).
[4] F. X. Zhang, M. Lang, R. C. Ewing, J. Lian, Z. W. Wang, J. Hu, and L. A. Boatner, J. Solid State Chem. **181**, 2633 (2008).
[5] M. B. Smirnov, A. P. Mirgorodsky, V. Y. Kazimirov, and R. Guinebretiere, Phys. Rev. B **78**, 094109 (2008).
[6] D. Errandonea and F. J. Manjón, Prog. Mater. Sci. **53**, 711 (2008).
[7] K. Kusaba, T. Yagi, M. Kikuchi, and Y. Syono, J. Phys. Chem. Solids **47**, 675 (1986).
[8] M. Lang, F. Zhang, J. Lian, C. Trautmann, R. Neumann, and R. C. Ewing, Earth Planet. Sci. Lett. **269**, 291 (2008).
[9] L. Li, Y. Su, and G. Li, Appl. Phys. Lett. **90**, 054105 (2007).
[10] F. J. Manjón (private communication).
[11] A. F. Reid and A. E. Ringwood, Earth Planet. Sci. Lett. **6**, 205 (1969).
[12] L. Liu, Earth Planet. Sci. Lett. **44**, 390 (1979).
[13] S. Ono, Y. Tange, I. Katayama, and T. Kikegawa, Am. Mineral. **89**, 185 (2004).
[14] E. Knittle and Q. Williams, Am. Mineral. **78**, 245 (1993).
[15] W. van Westrenen, M. R. Frank, J. M. Hanchar, Y. Fei, R. J. Finch, and C.-S. Zha, Am. Mineral. **89**, 197 (2004).
[16] K. Kusaba, Y. Syono, M. Kikuchi, and K. Fukuoka, Earth Planet. Sci. Lett. **72**, 433 (1985).
[17] M. Marqués, M. Flórez, J. M. Recio, L. Gerward, and J. Staun Olsen, Phys. Rev. B **74**, 014104 (2006).
[18] M. Marqués, J. Contreras-García, M. Flórez, and J. M. Recio, J. Phys. Chem. Solids **69**, 2277 (2008).
[19] V. P. Dmitriev, S. B. Rochal, Y. M. Gufan, and P. Tolédano, Phys. Rev. Lett. **60**, 1958 (1988).
[20] M. Catti, Phys. Rev. Lett. **87**, 035504 (2001).
[21] H. T. Stokes and D. M. Hatch, Phys. Rev. B **65**, 144114 (2002).
[22] D. Errandonea, EPL **77**, 56001 (2007).
[23] C. C. López, Ph.D. thesis, Universidad del País Vasco, 2006.
[24] M. I. Aroyo, J. M. Perez-Mato, C. Capillas, E. Kroumova, S. Ivantchev, G. Madariaga, A. Kirov, and H. Wondratschek, Z. Kristallogr. **221**, 15 (2006).
[25] M. I. Aroyo, A. Kirov, C. Capillas, J. M. Perez-Mato, and H. Wondratschek, Acta Crystallogr., Sect. A: Found. Crystallogr. **62**, 115 (2006).
[26] S. L. Chaplot, L. Pintschovius, N. Choudhury, and R. Mittal, Phys. Rev. B **73**, 094308 (2006).
[27] R. J. Finch and J. M. Hanchar, in *Zircon*, edited by J. M. Hanchar and P. W. O. Hoskin [Rev. Miner. Geochem. **53**, 1 (2003)].
[28] W. C. Tennant, R. F. C. Claridge, C. J. Walsby, and N. S. Lees, Phys. Chem. Miner. **31**, 203 (2004).
[29] G. Kresse and J. Furthmuller, Phys. Rev. B **54**, 11169 (1996).
[30] G. Kresse and D. Joubert, Phys. Rev. B **59**, 1758 (1999).
[31] J. P. Perdew and Y. Wang, Phys. Rev. B **45**, 13244 (1992).
[32] D. M. Ceperley and B. J. Alder, Phys. Rev. Lett. **45**, 566 (1980).
[33] H. J. Monkhorst and J. D. Pack, Phys. Rev. B **13**, 5188 (1976).
[34] M. A. Blanco, E. Francisco, and V. Luaña, Comput. Phys. Commun. **158**, 57 (2004).
[35] I. Farnan, E. Balan, C. J. Pickard, and F. Mauri, Am. Mineral. **88**, 1663 (2003).
[36] H. P. Scott, Q. Williams, and E. Knittle, Phys. Rev. Lett. **88**, 015506 (2001).
[37] S. Ono, K. Funakoshi, Y. Nakajima, Y. Tange, and T. Katsura, Contrib. Mineral. Petrol. **147**, 505 (2004).
[38] M. Marqués, J. Osorio, R. Ahuja, M. Flórez, and J. M. Recio, Phys. Rev. B **70**, 104114 (2004).
[39] H. Leroux, W. U. Reimold, C. Koeberl, U. Hornemann, and J.-C. Doukhan, Earth Planet. Sci. Lett. **169**, 291 (1999).
[40] C. Giacovazzo, H. L. Monaco, D. Viterbo, F. Scordari *et al.*, *Fundamentals of Crystallography*, 1st ed. (Oxford Universtiy Press, New York, 1992).
[41] A. D. Becke and K. E. Edgecombe, J. Chem. Phys. **92**, 5397 (1990).
[42] B. Silvi and A. Savin, Nature (London) **371**, 683 (1994).
[43] J. Contreras-García, A. Martín Pendás, and J. M. Recio, J. Phys. Chem. B **112**, 9787 (2008).
[44] L. Gracia, J. Contreras-García, A. Beltrán, and J. M. Recio, High Press. Res. (to be published).
[45] I. Bytheway, R. J. Gillespie, T. H. Tang, and R. F. W. Bader, Inorg. Chem. **34**, 2407 (1995).
[46] *Space-Groups Symmetry*, edited by T. Hahn (Reidel, Dordrecht, Holland/Boston, 1983), Vol. A.